COMMUNICATION

Solid Halide Electrolytes with High Lithium-Ion Conductivity for Application in 4 V Class Bulk-Type All-Solid-State Batteries

Tetsuya Asano,* Akihiro Sakai, Satoru Ouchi, Masashi Sakaida, Akinobu Miyazaki, and Shinya Hasegawa

New lithium halide solid-electrolyte materials, Li_3YCl_6 and Li_3YBr_6, are found to exhibit high lithium-ion conductivity, high deformability, and high chemical and electrochemical stability, which are required properties for all-solid-state battery (ASSB) applications, particularly for large-scale deployment. The lithium-ion conductivities of cold-pressed powders surpass 1 mS cm^{-1} at room temperature without additional intergrain or grain boundary resistances. Bulk-type ASSB cells employing these new halide solid electrolyte materials exhibit coulombic efficiencies as high as 94% with an active cathode material of $LiCoO_2$ without any extra coating. These superior electrochemical characteristics, as well as their material stability, indicate that lithium halide salts are another promising candidate for ASSB solid electrolytes in addition to sulfides or oxides.

All-solid-state batteries (ASSBs) with inorganic solid electrolytes (SEs) are promising candidates for next-generation energy storage because they can, in principle, overcome[1] some of the limitations of lithium-ion batteries (LIBs).[2] The essential advantages of ASSBs arise from the nature of inorganic SEs,[1] for example, the single ion conducting nature and thermal stability enabling ASSBs to run at a high current for fast charging/discharging[3] and its nonfluidity enabling direct stacking of cell units to reduce the inactive volume of a battery package to achieve a high module energy density.[4] For commercial ASSB applications, particularly for large-scale deployment, SEs need to satisfy not only superior electrochemical characteristics that directly limit the battery performance but also chemical and mechanical properties that are suited for the large-scale fabrication process.[5] Currently, some sulfide,[3,6] oxide,[7] and borohydride[8] materials show high ionic conductivity[9] and are considered possible candidate materials. Sulfides are the most advanced, with high conductivities approaching[6b,c] or even surpassing[3,6a] those of organic liquid electrolytes, and its deformable mechanical properties[5] realize intimate 2D contact between SE-SE grains and SE-active material grains simply by cold-pressing. On the other hand, oxides are chemically stable[10] and are often considered ideal materials if the

high-temperature process can be eliminated during battery fabrication. It is, however, still challenging to find SE materials[9] that simultaneously satisfy all the requirements: high ionic conductivity, electrochemical stability, chemical stability, and deformability.

In this regard, halide materials are attractive due to the nature of halogen anions, though they have received relatively little attention. First, monovalent halogen anions more weakly interact with lithium ions than divalent sulfur or oxygen anions do; thus, fast lithium-ion transport is expected. The ionic radii of halogen anions are relatively large (r_{Cl^-} = 167 pm, r_{Br^-} = 182 pm, r_{I^-} = 206 pm, r_{O2^-} = 126 pm, r_{S2^-} = 170 pm for hexacoordinated anions[11]), leading to long ionic bond lengths[12] and high polarizabilities[13] from which high lithium-ion mobility as well as high deformability are expected. Furthermore, some inorganic halide salts, especially those with high ionicity, are stable in dry air even at high temperatures.[14] This causes the high electrochemical oxidation stability of chlorides and bromides as identified by density functional theory (DFT) calculations.[15] Despite these advantageous anionic characteristics, studies of halide SEs have been relatively scarce.[9] Halide materials with fluorite structures[16] or spinel structures[9,17] were studied in the 1970s–1980s, and their lithium-ion conductivity at room temperature was on the order of 10^{-6} S cm^{-1} or less. Although Li-M-Br (M = Al, In, Ga) were studied in the 1990s–2000s and a high lithium-ion conductivity of 10^{-3} S cm^{-1} was previously reported, they are faced with unstable high conductivity phase at room temperature and electrochemical instability leading to unstable battery operation.[18] Based on these previous studies, the halide electrolytes have often been recognized as the material system with low ionic conductivity and low stability.[19]

Here, lithium-ion-conducting halide solid electrolytes, Li_3YCl_6 (LYC) and Li_3YBr_6 (LYB), are found to satisfy high lithium-ion conductivity, electrochemical stability, chemical stability, and deformability, which sulfide or oxide SEs alone have not realized so far. We have focused on yttrium halides due to the high stability of YX_6^{3-} (X = Cl or Br) octahedrons[20] as well as the expected conduction path incorporated with each trivalent yttrium that offers two empty cation sites. Combined with the aforementioned advantageous halide characteristics, LYC and LYB exhibit high lithium-ion conductivity despite their anionic close-packed structures. Excellent bulk-type ASSB

Dr. T. Asano, Dr. A. Sakai, S. Ouchi, M. Sakaida, A. Miyazaki, S. Hasegawa
Technology Innovation Division
Panasonic Corporation
1006 Kadoma, Kadoma-shi, Osaka 571-8508, Japan
E-mail: asano.tetsuya001@jp.panasonic.com
The ORCID identification number(s) for the author(s) of this article can be found under https://doi.org/10.1002/adma.201803075.

**ADVANCED
SCIENCE NEWS**

www.advancedsciencenews.com
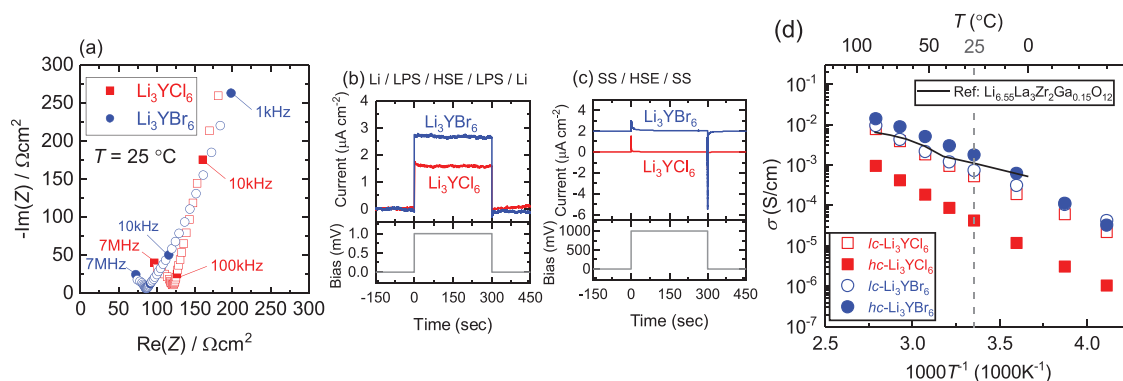
**ADVANCED
MATERIALS**

www.advmat.de

Figure 1. a) The Nyquist plots of the EIS measurement results of LYC and LYB with nonreversible electrodes. b,c) The transient current behavior under an applied DC bias on LYC and LYB either with lithium metal reversible electrodes or irreversible stainless-steel (SS) electrodes. Note that the plot of Li_3YBr_6 in (c) is vertically offset by 2 μA cm^{-2} and the bias applied in (c) is 1000 times higher than that in (b). d) Arrhenius conductivity plots of LYC and LYB. The open symbols (labeled lc) are mechanochemically synthesized samples without heat treatment. The solid symbols (labeled hc) are measured after annealing, grinding into powders and then cold-pressing. For comparison, the best reported garnet-type oxide SE (black)[7a] is plotted together.

performance is exhibited with $LiCoO_2$ (LCO) as a cathode active material without the need for external coating due to the high electrochemical stability of halide SEs.

The halide SEs, LYC and LYB, were mechanochemically synthesized from a stoichiometric mixture of binary compound precursors, LiCl and YCl_3 for LYC and LiBr and YBr_3 for LYB. The ionic conductivities of compressed powders of the LYC and LYB were measured using electrochemical impedance spectroscopy (EIS), and their Nyquist plots are shown in **Figure 1**a. Only one conductive impedance component is observed in the measured frequency range up to 7 MHz, and the result can be attributed to the total impedance including the bulk component and the grain boundary component if it exists. The conductivities at room temperature were 0.51 mS cm^{-1} for LYC and 0.72 mS cm^{-1} for LYB. To confirm whether the conducting carriers are lithium ions, we performed a DC measurement of LYC or LYB sandwiched by Li_2S-P_2S_5 (LPS) glass ceramic SE and Li-metal. The DC current continued to flow at a constant value (Figure 1b), and the resistance during the DC measurement was consistent with that of the AC impedance measurement (Figure S1a, Supporting Information). Since LPS is known to conduct only lithium ions, the conducting species of LYC and LYB should also be lithium ions, which was confirmed by another DC measurement on LYC or LYB with stainless-steel electrodes, in which the current quickly decayed to zero (Figure 1c), ruling out any major contribution to the conductivity from electrons. The electronic conductivity measured by the Hebb–Wagner polarization method[6b,21] was 2.8 × 10^{-9} S cm^{-1} for LYC and 1.0 × 10^{-9} S cm^{-1} for LYB (Figure S1b, Supporting Information), which are more than five orders of magnitude lower than the lithium-ion conductivity. Therefore, the conductivities of LYC and LYB measured in Figure 1a are indeed lithium-ion conductivity. The Arrhenius plots of the conductivities of LYC (red open square) and LYB (blue open circle) are shown in Figure 1d. The conductivities of LYC and LYB approach the best garnet-type oxide SE.[7a] Their activation energies are 0.40 eV for LYC and 0.37 eV for LYB. All the conductivity measurements of LYC and LYB were performed on pellets formed by simply cold-pressing powders with no heat treatment, indicating the highly deformable

characteristics of LYC and LYB, which are suitable for large-scale ASSB fabrication without a high-temperature process.[5b]

To identify the crystalline structure of the LYC and LYB, powder X-ray diffraction (XRD) patterns were taken, and the results are shown in **Figure 2**a,b. While some of the prominent diffraction peaks were observed, the peaks were broad, indicating low crystallinity (hereafter referred to as lc-LYC and lc-LYB) and hindering analysis of the detailed crystal structure. To obtain a high crystallinity specimen, the mechanochemically synthesized lc-LYC and lc-LYB were subsequently annealed, and we obtained highly crystalline LYC and LYB specimens (to be referred to as hc-LYC and hc-LYB), as shown in Figure 2c,d. We performed Rietveld analysis to identify the crystal structures of hc-LYC (Figure S2a and Table S1, Supporting Information) and hc-LYB (Figure S2b and Table S2, Supporting Information). The refined structures are shown in Figure 2e,f and in more detail in Figures S3 and S4 (Supporting Information). Evidently, LYC and LYB are isomorphs of Li_3ErCl_6 (ICSD No. 50151, space group $P\bar{3}m1$) and Li_3ErBr_6 (ICSD No. 50182, space group $C2/m$), respectively. Both LYC and LYB consist of the close-packed-like anion sublattice. LYC consists of a hexagonal close-packed (hcp)-like anion arrangement, while LYB consists of a cubic close-packed (ccp)-like anion arrangement. In both cases, yttrium resides at octahedral sites. Since the lithium sites are also octahedral sites, all the cations are located at octahedral sites. Therefore, the crystal structures of LYC and LYB can be considered the distorted NiAs structure and distorted rock-salt structure, respectively, in which one-third of the cation sites are inherently left vacant in both cases.

Detailed crystal structures of lc-LYC and lc-LYB cannot currently be determined due to their highly disordered signatures of the XRD patterns (Figure 2a,b). However, certain characteristics can be derived. They ought to belong to the same parent structures of hc-LYC and hc-LYB because all the peaks of lc-LYC and lc-LYB exist as peaks of hc-LYC and hc-LYB. The peak intensity ratio can be reproduced by disordered yttrium distribution, in which yttrium is distributed to different octahedral sites, while the anion framework structure shows no essential difference from that of the structure with high crystallinity (Figure S5, Tables S3 and S4, Supporting Information).
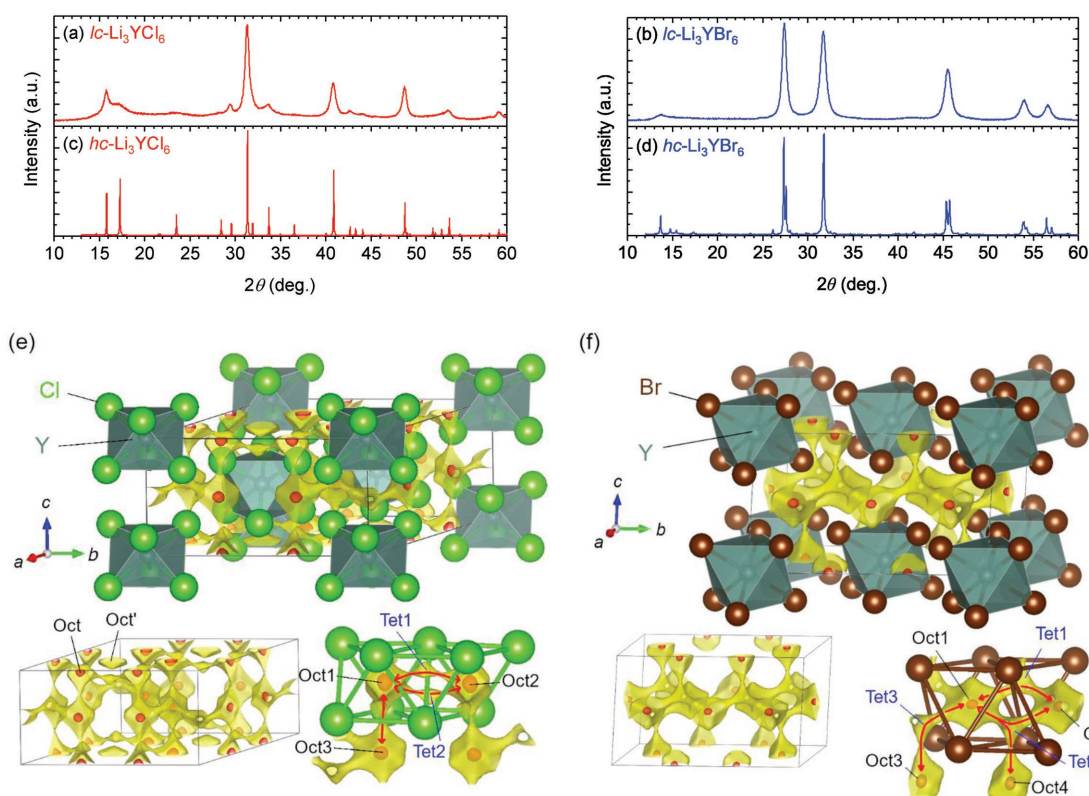
ADVANCED
SCIENCE NEWS
www.advancedsciencenews.com

ADVANCED
MATERIALS
www.advmat.de

Figure 2. a–d) The measured XRD patterns of mechanochemically synthesized lc-LYC (a), mechanochemically synthesized lc-LYB (b), annealed hc-LYC (c), and annealed hc-LYB (d). e,f) The crystal structures of LYC and LYB obtained after Rietveld refinement, superimposed with a calculated BVSE-based lithium-ion potential map. The yellow surface corresponds to the ionic conduction path, and the regions enclosed with red surfaces correspond to the stable lithium-ion positions. The crystal structures and potential isosurfaces are visualized using VESTA.[35]

The observed selective profile broadening of the peaks may be an indication of the introduction of high density planar defects (Figure S5, Supporting Information).[22] These can be considered circumstantial evidence of the partially disordered cation arrangement of mechanochemically synthesized lc-LYC and lc-LYB with essentially the same anion sublattice structures.

Notably, lithium ions are mobile at such high ionic conductivities in LYC and LYB despite the anion-close-packing structures, which is different from the conducting mechanism of sulfide SEs in which the body-centered cubic (bcc)-like arrangement of the anion sublattice is the key for high lithium-ion conductivity.[23] To elucidate the conduction paths in LYC and LYB structures, we calculated a 3D potential map of lithium ions in hc-LYC and hc-LYB based on a bond valence site energy (BVSE) method developed by Adams et al.[24] The two potential isosurfaces of lithium ions are drawn in Figure 2e,f and Figures S3 and S4 (Supporting Information); the yellow surfaces represent the simulated conduction path, and the red surfaces represent the stable lithium sites. For both LYC and LYB, stable lithium positions are located at the octahedral sites, which is consistent with the lithium sites determined by XRD Rietveld analysis. For LYC with an hcp-like anion arrangement, lithium-ion transport paths along the *ab*-plane are via tetrahedral interstitial sites (Oct1–[Tet1 or Tet2]–Oct 2 in Figure 2e), while along the *c*-axis, the paths are directly connected between neighboring octahedral sites (Oct1–Oct 3 in Figure 2e). For LYB, the lithium-ion conducting paths are connected via tetrahedral interstitial sites

in all three directions (Oct1–[Tet1 or Tet2]–Oct2, Oct1–Tet3–Oct3 in Figure 2f), reflecting upon ccp bromide ion arrangements. In both LYC and LYB, the tetrahedral interstitial sites adjacent to Y^{3+} are blocked by repulsive coulombic interactions between Y^{3+} and Li^+ (Figures S3b and S4b, Supporting Information), which is similar to the case for layered rock-salt cathode materials.[25] These pathways of lithium ions in LYC and LYB are in contrast to the highly conducting sulfides where lithium ions transport via face-shared distorted tetrahedral sites of a bcc-like anion arrangement.[23] This finding indicates that the material design principles for the high ionic conductivity of halide materials can be quite different from those of sulfides[23] or oxides.[7a,f]

The difference between the hcp-like anion arrangement of LYC and the ccp-like anion arrangement of LYB causes the contrasting relationship between lithium-ion conductivity and crystallinity. Interestingly, the conductivity of LYC decreased by improving the crystallinity, while that of LYB increased (Figure 1d). The room-temperature ionic conductivity of cold-pressed hc-LYB reached 1.7 mS cm^{-1}, which was 2–3 orders of magnitude higher than the previously studied halide electrolytes[9,19] and was even higher than that of the garnet-type oxide SE.[7a] This contrast between LYC and LYB can presumably be attributed to the difference in anion sublattice structures. For the case of LYC, due to the short cation–cation distance along the *c*-axis (≈3.01 Å as opposed to 3.97 Å for LYB), the repulsive interaction between Y^{3+} and Li^+ renders the octahedral

ADVANCED
SCIENCE NEWS
www.advancedsciencenews.com

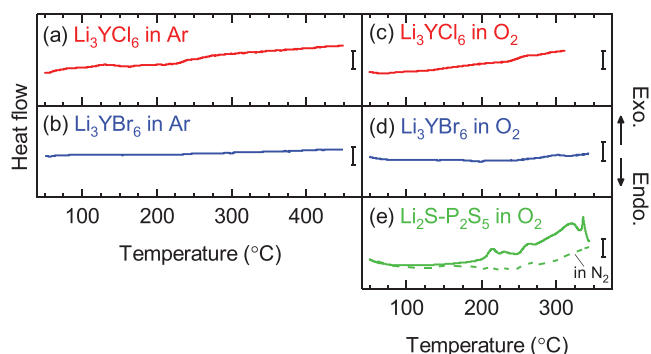**ADVANCED**
MATERIALS
www.advmat.de

Figure 3. a–d) The DSC measurements of LYC and LYB in an inert (Ar) atmosphere or in a dry oxygen atmosphere. The bars indicate the scale of 0.2 W g^{-1}. e) The same DSC measurement on LPS in an O$_2$ atmosphere compared with that in an N$_2$ inert atmosphere.

sites neighboring to Y^{3+} sites unfavorable, as shown by the absence of the red surface at Oct' in Figure 2e and Figure S3 (Supporting Information). This blocking by Y^{3+} may be relaxed at low crystallinity with a partially disordered structure,[22] and the conductivity improved with disordered lc-LYC. On the other hand, in LYB, a 3D network of conducting paths is formed in the hc-LYB structure with all the octahedral sites other than Y^{3+} sites almost equally available for lithium ions, which is probably the reason for the improved ionic conductivity of LYB with higher crystallinity by annealing. Further investigations are needed regarding the detailed crystal structures and conducting pathways for lc-LYC and lc-LYB.

Having demonstrated the high lithium-ion conductivity of LYC and LYB with cold-pressed pellets, we evaluated their material stability by differential scanning calorimetry (DSC) measurements in an inert atmosphere (**Figure 3**a,b) and in an oxygen atmosphere (Figure 3c,d). In both an inert atmosphere and an oxygen atmosphere, neither exothermic nor endothermic peaks are observed, indicating no thermal decomposition, phase transition, or oxidation reaction occurred within the measured temperature range, which is a clear indication of the high thermal and oxidation stability of LYC and LYB. Moreover, DSC measurement on the glass-ceramics LPS in an O$_2$ atmosphere shows some exothermic peaks that are not observed in N$_2$ atmosphere (Figure 3e), indicating oxidation reactions. These DSC measurement results are consistent with our estimation of the energy change in the oxidation reaction of several SEs using DFT calculations (Figure S6, Supporting Information). The calculated exothermic heat generated from the oxidation reaction of LYC and LYB is 20–100 times lower than those of high-conductivity sulfide materials (Figure S6, Supporting Information). This stability against oxygen is an important aspect for electrolytes,[26] although it has scarcely been studied for SEs, and their stability in oxygen may reduce the level of atmospheric control in their fabrication process and battery design.[5a]

The bulk-type ASSBs using LYC and/or LYB as SEs showed excellent performance in terms of its coulombic efficiency and cycle performance using 4 V class cathode active materials. To investigate battery performance using LYC and/or LYB, two types of bulk-type ASSB cells were fabricated (**Figure 4**a). One consisted of a mixture of LiCoO$_2$ (LCO) and LYC as the cathode layer, LYC as the SE layer, and In-Li alloy[6b,27] as the reference

electrode (referred to as LYC-cell hereafter). The other is the same as the LYC-cell but with LYB in place of the LYC of SE layer (referred to as LYC/LYB-cell hereafter). These ASSB cells were fabricated out of LCO and SE powders (LYC and/or LYB) simply by a standard cold-press method (see the Experimental Section for details about the cell design and fabrication process).[28] The charge/discharge curves at the initial cycle of these cells are shown in Figure 4a. The initial charge and discharge curves almost follow the LCO electromotive force (EMF) curve, indicating that almost no side reactions occur in this battery configuration. The initial coulombic efficiency is 94.8% for LYC-cell and 94.2% for LYC/LYB-cell. Such a high coulombic efficiency is a clear indication that the LYC is highly stable against 4 V class cathode active materials as opposed to the previous recognition of halide materials to be low oxidation stabilities.[19] To shed light on the charging process of the LYC-cell, we took an in situ XRD pattern during the initial charging cycle, and its results are shown in Figure 4b and Figure S7 (Supporting Information). As the lithium is extracted from LCO, the LCO (003), (006), and (104) peaks shifted to a lower angle while (101) peak shifted slightly toward a higher angle (Figure 4b), indicating the c-axis of the LCO is elongated while the a-axis is shortened as quantitatively shown in Figure S7e (Supporting Information), which is consistent with the previously reported LCO behavior measured in situ with liquid electrolytes.[29] However, no peak shifts were observed for LYC. Therefore, this in situ XRD result is another confirmation that the charging current is solely based on Li$^+$ extraction from LCO. Figure 4c is a scanning electron microscopy (SEM) image of the LYC-cell. The LYC is highly deformed and compliant to LCO particles to fill up the open spaces, and 2D contact areas were formed.

Notably, no coating on the LCO powders was used in the ASSB cells in this study, and yet, a high battery performance was obtained for the LYC-cell and the LYC/LYB-cell, which is in contrast to the results for the sulfide SEs in which extra oxide coating on the cathode materials is needed to achieve enhanced battery performance.[30] The coulombic efficiencies in the initial cycle are much higher for the LYC-cell (94.8%) and the LYC/LYB-cell (94.2%) than for the SSE-cell (84.0%). At the beginning of the initial charging cycle of the SSE-cell, the potential gradually increased to reach the potential plateau of LCO (Figure S8, Supporting Information), indicating loss of lithium from the sulfide SE.[30] On the other hand, no such behavior was observed either in the LYC-cell or in the LYC/LYB-cell (Figure S8, Supporting Information). The interfacial resistance between LCO and LYC was only 16.8 Ω cm^2 for the LYC-cell and 6.6 Ω cm^2 for the LYC/LYB-cell, which are much smaller values than 128.4 Ω cm^2 of the SSE-cell (Figure 4d and Figure S9, Supporting Information). Nonrequirement of extra coating on LCO is another indication of the oxidation stability of LYC and LYB, which originated from the higher electrochemical stabilities of chlorine and bromine ions than of sulfur ions. This is consistent with first-principles calculation results of thermodynamic electrochemical window of some other chlorides or bromides.[15a]

The ASSB cells using an LYC and/or LYB electrolyte also showed reasonable rate capability and cycle performance. As shown in Figure 4e, the discharge capacity of both the LYC-cell and the LYC/LYB-cell retain more than 40% at a high current density up to 5 C compared to that of 0.1 C. Given the internal
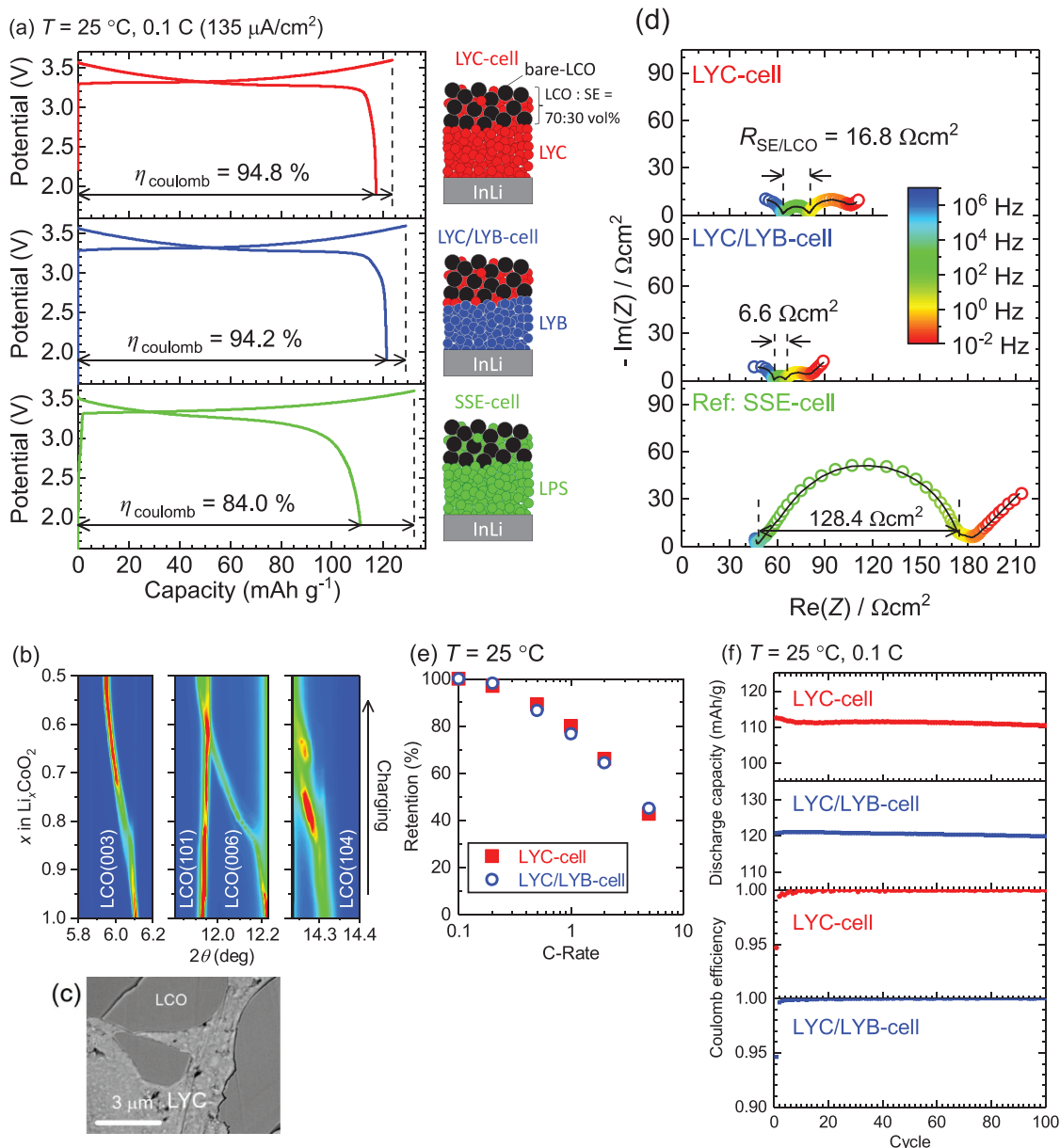
**ADVANCED
SCIENCE NEWS**

www.advancedsciencenews.com

**ADVANCED
MATERIALS**

www.advmat.de

Figure 4. a) Initial charge/discharge curves of bulk-type ASSB cells at 25 °C at 0.1 C. The schematic cell structures are drawn on the right side of each plot. b) In situ XRD measurement results of the LYC-cell during initial charging. c) The cross-sectional SEM image of the cathode layer. d) The Nyquist plots of the EIS spectra of ASSB cells after the first charging cycle. Open circles are the measured plot color-coded with the frequency. Black lines are the fitted curve using the equivalent circuit model (Figure S9, Table S6, Supporting Information). e) The relative discharge capacities of different C-rates with respect to 0.1 C. f) The discharge capacity retention and coulombic efficiency of the LYC-cell and the LYC/LYB-cell for 100 cycles.

resistance of the cells shown in Figure 4d, these rate capabilities are reasonable without excessive degradation at high current. Figure 4f shows the coulombic efficiency and the retention of the discharge capacity for 100 cycles. After the initial cycle, the coulombic efficiency is higher than 99%, and after the tenth cycle and onward, it is above 99.9%, leading to a high cycle performance, and the retained discharge capacity at the 100th cycle is 98.0%. The high ASSB performance proves that the halide materials LYC and LYB are promising candidates for ASSB applications.

In conclusion, we demonstrated for the first time that new halide SEs, LYC and LYB, are suitable for bulk-type ASSBs in

terms of their electrochemical and mechanical characteristics and their chemical stability. The lithium-ion conductivities of cold-pressed pellets reached 0.51 mS cm^{-1} for LYC and 1.7 mS cm^{-1} for LYB at room temperature; the latter is even higher than the best reported oxide garnet-type lithium-ion conductors. Interestingly, such high conductivity was realized in their close-packed anion sublattice, which is unlike the origin for high lithium-ion conductivity for sulfide[23] or oxide[7a,f] lithium-ion conductors. The bulk-type ASSB cells using LYC and/or LYB fabricated by a simple cold-pressed method show excellent charge/discharge characteristics, namely, high initial

**ADVANCED
SCIENCE NEWS**
www.advancedsciencenews.com

**ADVANCED
MATERIALS**
www.advmat.de

coulombic efficiency of 94%, low interfacial resistance between LCO and SE, and satisfactory cycling performance. Notably, the high ASSB performance was realized with a 4 V class LCO cathode active material without any extra coating, which is due to the high oxidation stability of chlorides and bromides. Concerning the material availability of yttrium, its elemental abundance in earth's crust is 30–33 g ton^{-1}, which is comparable to or higher than that of cobalt even after normalized with atomic mass.[31] All the above features indicate not only that LYC and LYB are promising candidates for the SEs for bulk-type ASSBs particularly for large-scale applications, but also that halide materials in general hold high possibilities as SEs for ASSBs other than the current mainstream sulfide and oxide materials.

Experimental Section

Material Synthesis: The starting materials are binary halide materials, LiCl (>99.9%, Kojundo Kagaku) and YCl$_3$ (>99.9%, Sigma-Aldrich) for LYC or LiBr (>99.9%, Kojundo Kagaku) and YBr$_3$ (>99.9%, Alfa-Aesar) for LYB, which were weighed in a molar ratio of LiCl/YCl$_3$ = 3/1 for LYC or LiBr/YBr$_3$ = 3/1 for LYB and loaded into zirconia pots with ϕ 5 mm zirconia balls. These preparations were conducted in an argon-filled glove box, and the zirconia pots were sealed in argon. The mixed starting materials were mechanochemically milled with planetary ball milling for 50 h over 500 rpm.[32] This procedure results in white powders of lc-LYC and lc-LYB. The resultant materials are hygroscopic and need to be dealt with in dry atmosphere. For hc-LYC and hc-LYB synthesis, the mechanochemically synthesized powders were sealed in a vacuum quartz tube and subsequently annealed at 550 °C. The compositions of the resultant materials were measured with inductively coupled plasma optical emission spectroscopy (ICP-OES) and atomic absorption spectrometry (AAS), and confirmed to be identical to the intended composition within 1%. LPS was mechanochemically synthesized from premixed Li$_2$S/P$_2$S$_5$ with a 75/25 molar ratio using planetary ball milling at 510 rpm for 40 h, followed by heat treatment at 270 °C for 2 h.[5b]

Material Characterization: The crystal structure of the synthesized materials was characterized by XRD using Cu Kα1 radiation by SmartLab (Rigaku Co.) using the Bragg–Brentano method in a dry air atmosphere (dew point less than −50 °C). The X-ray was monochromated by Johansson monochromator with Ge (111) reflection. The measured spectra were analyzed by the Rietveld method using RIETAN-FP.[33] The DSC measurements were carried out using EXSTAR6000 differential scanning calorimetry (Seiko Instrument Inc.). ≈10 mg of specimen was loaded into a stainless-steel capsule and sealed in either an argon atmosphere or an O$_2$ atmosphere. α-Al$_2$O$_3$ powder sealed in a stainless-steel capsule was used as a reference. The temperature was scanned at a rate of 10 °C min^{-1}.

Electrochemical Characterizations: The electrochemical characterization including EIS and DC measurements of LYC and LYB were performed on a cold-pressed pellet of powders without heat treatment. The annealed samples were first ground into powder and then cold-pressed for the measurements. The synthesized powder was loaded in an electrically insulating cylindrical cell with an inner diameter of φ 9.5 mm and was subsequently compressed under 300 MPa. For the measurements with stainless-steel electrodes, the pellets were simply sandwiched by two stainless-steel electrodes. The amount of the specimen loaded for the measurements with stainless-steel electrodes were ≈100 mg for LYC and 150 mg for LYB, resulting in ≈600 µm of thickness after compression. The Hebb–Wagner polarization method was performed on Au/LYC or LYB/InLi cell. For the measurements with the Li-metal electrodes, LPS electrolyte powders were inserted and then pressed before placing Li-metal electrodes to block both the electrons and any other ions than lithium ions. The EIS measurements were performed in a frequency range between 7 MHz and 10 mHz with a 10 mV driving potential amplitude with respect to the open-circuit voltage. All the above measurements, the EIS measurements and the DC measurements, were performed

using a BioLogic VSP300 instrument at the temperature of 25 °C unless otherwise noted. The temperature was controlled by placing the cells in a temperature chamber (ESPEC Co., SU-241) during measurement. The conductivity value is obtained by the standard formula, $\sigma = t/RA$, where t is the thickness of the pellet, A is the area of the pellet, and R is the resistance value obtained from the EIS measurement. The values of R were taken from the real part of impedance whose absolute value of imaginary part was lowest. This value of R was confirmed to be identical with the value obtained by fitting to equivalent circuit model within 1%.

BVSE Calculation: The empirical BVSE calculation was performed two ways, namely, using *soft*BV software tool with updated potential parameters[24b,34] and using MATLAB with a self-written code following ref. [24a]. Both methods essentially produced identical results in terms of the expected ionic conduction path and the stable lithium positions. The potential energy of Li$^+$ is obtained by summing up the classical interatomic potential of Li$^+$ exerted from other immobile ions (Y^{3+}, Cl$^-$, and Br$^-$ in this study) in real space based on predetermined potential parameters. The interaction between Li$^+$ and Cl$^-$ or Br$^-$ is based on the Morse-type potential, and the interaction between Li$^+$ and Y^{3+} is based on coulombic repulsive interactions with consideration of the partial effective oxidation states. The grid size of the calculation was 0.1 Å.

ASSB Cell Fabrication and Battery Performance Measurement: The specifications for ASSB cells are summarized in **Table 1**. All LYC and LYB used for ASSB cells were lc-LYC and lc-LYB. The positive electrode mixture was prepared by mixing LCO and LYC with LCO:LYC = 82.4:17.6 in a gravimetric ratio, which translates to LCO:LYC = 70:30 as a volume ratio. Then, 50 mg of LYC powder or 100 mg of LYB powder, 8.5 mg of a positive electrode mixture of LCO–LYC, and 16 mg of aluminum powders as positive current collector together were pressed under 300 MPa to form disc-shaped pellets 9.5 mm in diameter. Li-In alloy[6b,27] whose potential was confirmed to be stable at +0.62 V versus Li/Li$^+$ was used as a negative electrode instead of Li metal to avoid the evaluation of battery performance being limited by known issues related to plating/deplating of Li metal on solid electrolytes.[1] Stainless-steel current collectors were connected to the cathode and anode. This cell design amounts to a theoretical capacity of 1.35 mAh cm^{-2} in a 0.5 electron reaction for LCO. The thickness of reference negative electrode is more than sufficient to maintain the constant potential after acceptance of all the lithium from cathode side during charging process. These cell fabrication processes were conducted in argon atmosphere with dew point less than −60 °C. Charge/discharge measurements were carried out in constant current mode terminated at 3.6 V for charging and 1.9 V for discharging. For the rate-performance measurements in Figure 4e, all the charging cycles were at 0.1 C which corresponds to 135 µA cm^{-2}, and the discharging current was increased each cycle; 0.1 C → 0.2 C → 0.5 C → 1 C → 2 C → 5 C. For the cycling measurement in Figure 4f, both the charging cycle and discharging cycle were at 0.1 C. The temperature for all the battery performance measurements were at $T = 25$ °C.

Table 1. The specifications of ASSB cells.

Specifications	LYC-cell	LYC/LYB-cell
Mass loading of LCO [mg cm^{-2}]	9.9	9.9
Theoretical cell capacity [mAh cm^{-2}]	1.35[a]	1.35[a]
The volumetric mixture ratio of LCO:LYC in cathode layer	70:30	70:30
The gravimetric mixture ratio of LCO:LYC in cathode layer	82:18	82:18
Cathode layer thickness [µm]	42[b]	42[b]
SE layer thickness [µm] (estimated packing density[c])	350 (0.82)	460 (0.84)
Li:In molar ratio	38:62	38:62
The thicknesses of Li/In [µm]	200/400	200/400

[a]For 0.5 electron reaction per LiCoO$_2$ formula unit; [b]The estimated packing density is 0.68; [c]The packing densities were estimated based on the resultant thickness of the layer and the loaded materials amount.

In Situ XRD Measurements: The cell for the in situ XRD measurement was prepared in the same manner as the aforementioned ASSB cell fabrication process, but the pellet was extracted from the cylindrical cell after fabrication. The cell pellet was then sealed in an aluminum laminated package with leads for the positive and negative electrodes. In situ XRD measurements were performed using a synchrotron radiation source at the beamline BL16XU at SPring-8. The X-ray energy was 24.8 keV, and the measurement was conducted using asymmetric reflection geometry. More details of the measurement are described in Supporting Information.

Conflict of Interest

The authors declare no conflict of interest.

[1] J. Janek, W. G. Zeier, *Nat. Energy* **2016**, *1*, 16141.

[2] a) M. Armand, J. M. Tarascon, *Nature* **2008**, *451*; b) J. M. Tarascon, M. Armand, *Nature* **2001**, *414*, 359; c) J. B. Goodenough, K. S. Park, *J. Am. Chem. Soc.* **2013**, *135*, 1167.

[3] Y. Kato, S. Hori, T. Saito, K. Suzuki, M. Hirayama, A. Mitsui, M. Yonemura, H. Iba, R. Kanno, *Nat. Energy* **2016**, *1*, 16030.

[4] Y. J. Nam, S. J. Cho, D. Y. Oh, J. M. Lim, S. Y. Kim, J. H. Song, Y. G. Lee, S. Y. Lee, Y. S. Jung, *Nano Lett.* **2015**, *15*, 3317.

[5] a) J. Schnell, T. Günther, T. Knoche, C. Vieider, L. Köhler, A. Just, M. Keller, S. Passerini, G. Reinhart, *J. Power Sources* **2018**, *382*, 160; b) A. Sakuda, A. Hayashi, M. Tatsumisago, *Sci. Rep.* **2013**, *3*, 2261.

[6] a) Y. Seino, T. Ota, K. Takada, A. Hayashi, M. Tatsumisago, *Energy Environ. Sci.* **2014**, *7*, 627; b) N. Kamaya, K. Homma, Y. Yamakawa, M. Hirayama, R. Kanno, M. Yonemura, T. Kamiyama, Y. Kato, S. Hama, K. Kawamoto, A. Mitsui, *Nat. Mater* **2011**, *10*, 682; c) D. Hans-Jörg, K. Shiao-Tong, E. Hellmut, V. Julia, R. Christof, Z. Torsten, S. Marc, *Angew. Chem., Int. Ed.* **2008**, *47*, 755.

[7] a) C. Bernuy-Lopez, W. Manalastas, J. M. Lopez del Amo, A. Aguadero, F. Aguesse, J. A. Kilner, *Chem. Mater.* **2014**, *26*, 3610;

[b)] C. A. Geiger, E. Alekseev, B. Lazic, M. Fisch, T. Armbruster, R. Langner, M. Fechtelkord, N. Kim, T. Pettke, W. Weppner, *Inorg. Chem.* **2011**, *50*, 1089; c) Y. Inaguma, C. Liquan, M. Itoh, T. Nakamura, T. Uchida, H. Ikuta, M. Wakihara, *Solid State Commun.* **1993**, *86*, 689; d) C. Ma, Y. Cheng, K. Chen, J. Li, B. G. Sumpter, C.-W. Nan, K. L. More, N. J. Dudney, M. Chi, *Adv. Energy Mater.* **2016**, *6*, 1600053; e) G. Adachi, N. Imanaka, H. Aono, *Adv. Mater.* **1996**, *8*, 127; f) K. Fujimura, A. Seko, Y. Koyama, A. Kuwabara, I. Kishida, K. Shitara, C. A. J. Fisher, H. Moriwake, I. Tanaka, *Adv. Energy Mater.* **2013**, *3*, 980.

[8] H. Maekawa, M. Matsuo, H. Takamura, M. Ando, Y. Noda, T. Karahashi, S.-I. Orimo, *J. Am. Chem. Soc.* **2009**, *131*, 894.

[9] J. C. Bachman, S. Muy, A. Grimaud, H.-H. Chang, N. Pour, S. F. Lux, O. Paschos, F. Maglia, S. Lupart, P. Lamp, L. Giordano, Y. Shao-Horn, *Chem. Rev.* **2016**, *116*, 140.

[10] Y. Deng, C. Eames, J.-N. Chotard, F. Lalère, V. Seznec, S. Emge, O. Pecher, C. P. Grey, C. Masquelier, M. S. Islam, *J. Am. Chem. Soc.* **2015**, *137*, 9136.

[11] R. D. Shannon, *Acta Crystallogr. Sect. A* **1976**, *32*, 751.

[12] L. Pauling, *The Nature of the Chemical Bond and the Structure of Molecules and Crystals: An Introduction to Modern Structural Chemistry*, Cornell University Press, New York **1960**, pp. 505–562.

[13] N. W. Ashcroft, N. D. Mermin, *Solid State Physics*, Holt, Rinehart and Winston, New York **1976**, pp. 533–559.

[14] S. H. White, in *Molten Salt Techniques*, Vol. 1 (Eds: R. J. Gale, D. G. Lovering), Plenum, New York **1983**.

[15] a) W. D. Richards, L. J. Miara, Y. Wang, J. C. Kim, G. Ceder, *Chem. Mater.* **2015**, *28*, 266; b) Y. Zhu, X. He, Y. Mo, *ACS Appl. Mater. Interfaces* **2015**, *7*, 23685.

[16] P. Hartwig, W. Weppner, W. Wichelhaus, *Mater. Res. Bull.* **1979**, *14*, 493.

[17] R. Kanno, Y. Takeda, O. Yamamoto, *Solid State Ionics* **1988**, *28*, 1276.

[18] a) Y. Tomita, H. Matsushita, K. Kobayashi, Y. Maeda, K. Yamada, *Solid State Ionics* **2008**, *179*, 867; b) Y. Tomita, H. Ohki, K. Yamada, T. Okuda, *Solid State Ionics* **2000**, *136*, 351.

[19] A. Manthiram, X. Yu, S. Wang, *Nat. Rev. Mater.* **2017**, *2*, 16103.

[20] G. N. Papatheodorou, *J. Chem. Phys.* **1977**, *66*, 2893.

[21] B. J. Neudecker, W. Weppner, *J. Electrchem. Soc.* **1996**, *143*, 2198.

[22] N. Yabuuchi, R. Hara, M. Kajiyama, K. Kubota, T. Ishigaki, A. Hoshikawa, S. Komaba, *Adv. Energy Mater.* **2014**, *4*, 1301453.

[23] Y. Wang, W. D. Richards, S. P. Ong, L. J. Miara, J. C. Kim, Y. Mo, G. Ceder, *Nat. Mater.* **2015**, *14*, 1026.

[24] a) S. Adams, R. P. Rao, *Phys. Status Solidi A* **2011**, *208*, 1746; b) H. M. Chen, S. Adams, *IUCrJ* **2017**, *4*, 614.

[25] J. Lee, A. Urban, X. Li, D. Su, G. Hautier, G. Ceder, *Science* **2014**, *343*, 519.

[26] P. Ribière, S. Grugeon, M. Morcrette, S. Boyanov, S. Laruelle, G. Marlair, *Energy Environ. Sci.* **2012**, *5*, 5271.

[27] K. Takada, N. Aotani, K. Iwamoto, S. Kondo, *Solid State Ionics* **1996**, *86*, 877.

[28] K. Iwamoto, N. Aotani, K. Takada, S. Kondo, *Solid State Ionics* **1995**, *79*, 288.

[29] J. N. Reimers, J. R. Dahn, *J. Electrchem. Soc.* **1992**, *139*, 2091.

[30] a) N. Ohta, K. Takada, I. Sakaguchi, L. Zhang, R. Ma, K. Fukuda, M. Osada, T. Sasaki, *Electrochem. Commun.* **2007**, *9*, 1486; b) N. Ohta, K. Takada, L. Zhang, R. Ma, M. Osada, T. Sasaki, *Adv. Mater.* **2006**, *18*, 2226.

[31] a) S. R. Taylor, *Geochim. Cosmochim. Acta* **1964**, *28*, 1273; b) Abundance of elements in the Earth's crust, https://en.wikipedia.org/wiki/Abundance_of_elements_in_Earth%27s_crust (accessed: July 2018).

[32] M. Tatsumisago, R. Takano, K. Tadanaga, A. Hayashi, *J. Power Sources* **2014**, *270*, 603.

[33] F. Izumi, K. Momma, *Solid State Phenom.* **2007**, *130*, 15.

[34] H. Chen, L. L. Wong, S. Adams, unpublished.

[35] K. Momma, F. Izumi, *J. Appl. Crystallogr.* **2011**, *44*, 1272.